Diverse genetic-driven immune landscapes dictate tumor progression through distinct mechanisms

Marco Bezzi[1,6], Nina Seitzer[1,6], Tomoki Ishikawa[1,6], Markus Reschke[1], Ming Chen[1], Guocan Wang[1], Caitlin Mitchell[1], Christopher Ng[1], Jesse Katon[1], Andrea Lunardi[1], Sabina Signoretti[2,3], John G. Clohessy[1,4], Jiangwen Zhang[5] & Pier Paolo Pandolfi[1]

[1]Cancer Research Institute, Beth Israel Deaconess Cancer Center, Department of Medicine, Beth Israel Deaconess Medical Center, Harvard Medical School, Boston MA 02115, USA

[2]Department of Pathology, Brigham and Women's Hospital, Boston, MA 02115, USA

[3]Department of Medical Oncology, Dana-Farber Cancer Institute, Boston, MA 02115, USA

[4]Preclinical Murine Pharmacogenetics Facility, Beth Israel Deaconess Medical Center, Harvard Medical School, Boston, Massachusetts, USA

[5]School of Biological Sciences, The University of Hong Kong, Hong Kong SAR, China

[6]These authors contributed equally to this work.

Correspondence should be addressed to P. P. P. (ppandolf@bidmc.harvard.edu).

Abstract

Multiple immune cell types can infiltrate tumors to promote progression and metastasis through different mechanisms, including immune-suppression. It is currently unclear how distinct genetic alterations in the tumor impact the composition of the immune landscape. Here, we have characterized the immune cell composition of prostate cancers driven by the loss of the critical tumor suppressor gene, Pten, either alone, or, in combination with the loss of *Trp53*, *Zbtb7a* or *Pml*. We found a striking quantitative and qualitative heterogeneity that is directly dependent on the specific genetic events in the tumor and ranges from "cold", non-inflamed tumors to massively infiltrated landscapes, with important therapeutic implications. Further, we show that these qualitative differences are observed in transcriptomic analysis of human prostate cancer samples. These data suggest that patient stratification on the basis of integrated genotypic-immune phenotypic analyses is needed for successful clinical trials and tailored precision immune therapies.

Introduction

The tumor microenvironment (TME) plays an important role in tumor progression and response to therapy[1-4], and immune checkpoint-targeting inhibitors are revolutionizing cancer therapy[5]. However in prevalent tumor types, such as prostate cancer, significant responses to checkpoint blockade has been only observed in subsets of patients, suggesting that both patient selection and combination therapy could be crucial[6-8]. In this regard, exploiting the role of innate immunity, which has been shown to play a key pro-tumoral role[9,10], has recently attracted considerable attention. The recruitment and function different types of immune cells in the TME change significantly during tumor evolution[1,3,11], in a process that seems to be strongly context-dependent[12,13], while "immune-desert" tumors have been also observed especially in patients resistant to immunotherapy[14]. Still, the precise determinants that trigger a specific immune landscape are not clear and it is currently unknown whether, or how, its evolution is directly driven by the genetic make-up of cancer, which in turn limits the precision of therapeutic immune interventions.

Here, we demonstrate that different genetic backgrounds in prostate cancer profoundly influence the composition of the TME. In particular, we characterized the nature and role of immune cell components of genetically engineered mouse models (GEMMs) of prostate cancer driven only by the loss of *Pten*[15], or the compound loss of *Pten* along with the loss of *Zbtb7a/Pokemon*[16], *p53*[17], or *Pml* tumor suppressors (the *Pten; Pml* prostate specific double null GEMM is described in Chen et al. *in press*). Our data support the notion that the integrated analysis of the genetic make-up and immune landscape of cancer is essential for the development of precision immunotherapy.

Results

The genetic make-up of prostate cancer dictates the composition of immune infiltrates in the primary tumor.

To address whether the genetic make-up of cancer impacts the component of the TME, we analyzed GEMMs driven by distinct genetic alterations representative of human prostate cancer[18,19]. In addition to the non-lethal *Pten*-loss driven mouse model (*Pten*$^{Lx/Lx}$;*Probasin-Cre*, prostate specific loss of PTEN; referred to as *Pten*$^{pc-/-}$), we characterized the composition of the immune cells in tumors from *Pten*$^{pc-/-}$;*Pml*$^{pc-/-}$, *Pten*$^{pc-/-}$;*Zbtb7a*$^{pc-/-}$ and *Pten*$^{pc-/-}$;*Trp53*$^{pc-/-}$ mice, which all display very aggressive phenotypes.

We first analyzed T cells (CD3+), B cells (CD19+/B220+), macrophages (CD11b+/F480+) and Gr-1+/CD11b+ myeloid cells (immature myeloid cells, monocytes, neutrophils) in whole prostate tumor at 3 months of age. At this age, all of the analyzed GEMMs developed high-grade prostatic intraepithelial neoplasia with locally invasive prostatic adenocarcinoma only observed in *Pten*$^{pc-/-}$;*Zbtb7a*$^{pc-/-}$, *Pten*$^{pc-/-}$;*Trp53*$^{pc-/-}$ and *Pten*$^{pc-/-}$;*Pml*$^{pc-/-}$ mice (Fig. 1a, b, black arrows). While we could not detect any changes in cell populations in the spleen between control and tumor bearing mice, or between different models (Supp. Fig. 1a), the primary tumor tissue showed profound differences in the immune cell infiltrates in the various GEMMs (Fig. 1c and Supp. Fig. 1b, c and d). Consistent with a previous report[20], Gr-1+/CD11b+ cells were increased in *Pten*$^{pc-/-}$ prostate tumors as compared to control prostates. Moreover, compound loss of *Zbtb7a* or *p53* further increased the accumulation of Gr-1+/CD11b+ cells, when compared to *Pten*$^{pc-/-}$ mice. By contrast, the infiltration of Gr-1+/CD11b+ cells as well as T cells was decreased in *Pten*$^{pc-/-}$;*Pml*$^{pc-/-}$ tumors compared to the other models (Fig. 1c, d and Supp. Fig. 1b).

Next, in order to understand how the immune landscape evolves during the progression of tumoral growth, we analyzed our prostate cancer models at 6 months of age. At this stage,

Pten$^{pc-/-}$*;Trp53*$^{pc-/-}$ mice displayed larger tumors compared to *Pten*$^{pc-/-}$*;Zbtb7a*$^{pc-/-}$ and *Pten*$^{pc-/-}$*;Pml*$^{pc-/-}$ mice (Fig. 1e). Remarkably, while we did not detect major changes in cell populations in the spleen of these tumor-bearing mice (Supp. Fig. 2a), the immune landscapes of the three models diverged even further in accordance with the profiles observed at 3 months of age (Fig. 1f and Supp. Fig 2b). The *Pten*$^{pc-/-}$*;Pml*$^{pc-/-}$ tumors still had a limited immune infiltrate, whereas the *Pten*$^{pc-/-}$*;Zbtb7a*$^{pc-/-}$ immune landscape was dominated by Gr-1+/CD11b+ cells. The Gr-1+/CD11b+ population was also increased in *Pten*$^{pc-/-}$*;Trp53*$^{pc-/-}$ mice along with a marked recruitment of T cells and macrophages. Interestingly, further analysis revealed that the majority of macrophages had an M2-like phenotype (CD11b+/F4/80+/CD206+) (Supp. Fig 2c) and that the increase of CD3+ cells reflected the recruitment of CD4+/FoxP3+ T regulatory cells (Treg), defining a potentially favorable microenvironment for cancer immune-evasion (Supp. Fig. 2d, e, f). These data indicate that the genetic make-up of prostate cancer determines the composition of the immune infiltrate in the primary tumor.

Characterization of Gr-1+/CD11b+ cells in *Pten*$^{pc-/-}$*;Zbtb7a*$^{pc-/-}$ and *Pten*$^{pc-/-}$*;Trp53*$^{pc-/-}$ prostate tumors.

The population of Gr-1+/CD11b+ cells is heterogeneous and comprises mature neutrophils, monocytes and immature myeloid cells (iMC). The latter, when able to suppress cytotoxic T cells, are functionally classified as myeloid derived suppressor cells (MDSCs)[21]. MDSCs can be further divided into polymorphonuclear MDSCs (PMN-MDSCs) and monocytic MDSCs (Mo-MDSCs) based on morphological analysis and on the expression of the markers Ly6C and Ly6G[13,21]. Thus, we determined the morphology of the tumor infiltrated Gr-1+/CD11b+ cells in the two models that showed the highest levels of infiltration of myeloid cells at 3 months of age (Fig. 2a). This analysis verified the partly hypersegmented granulocytic phenotype of the Gr-1+/CD11b+ cells in *Pten*$^{pc-/-}$*;Zbtb7a*$^{pc-/-}$, distinctive of PMN-MDSCs and neutrophils. In contrast, the *Pten*$^{pc-/-}$*;Trp53*$^{pc-/-}$ infiltrated Gr-1+/CD11b+ cell population appeared heterogeneous and

included both polymorphonuclear and mononuclear cells. Using immunohistochemistry (IHC) of the Ly6G epitope (Supp. Fig. 3a), we find that Ly6G+ cells reside mainly in the intra-epithelium of *Pten*$^{pc-/-}$*;Zbtb7a*$^{pc-/-}$ and *Pten*$^{pc-/-}$*;Trp53*$^{pc-/-}$ tumors. Strikingly, compared to IHC of other immune cell infiltrates (Supp. Fig. 3b) that were primarily located in the stroma, only Ly6G+ cells were detected in close proximity to tumor cells.

We next examined the expression level of a panel of genes implicated in the pro-tumoral function of myeloid cells[21]. The Gr-1+/CD11b+ cells in *Pten*$^{pc-/-}$ mice were recently shown to support prostate tumors by opposing the senescence response and also through classical immune suppression via Arginase 1 (Arg1) and inducible nitric oxidase (iNOS) expression[20,22]. Interestingly, Gr-1+/CD11b+ cells sorted from *Pten*$^{pc-/-}$*;Zbtb7a*$^{pc-/-}$ tumors showed low expression of Arg1 as well as iNOS, whereas Gr-1+/CD11b+ cells from *Pten*$^{pc-/-}$*;Trp53*$^{pc-/-}$ tumors showed high expression of Arg1 and low expression of iNOS when compared to Gr-1+/CD11b+ cells sorted from *Pten*$^{pc-/-}$ tumors (Fig. 2b). Notably, Gr-1+/CD11b+ cells sorted from *Pten*$^{pc-/-}$*;Zbtb7a*$^{pc-/-}$ tumors showed higher expression of the tumor promoting genes S100a9, S100a8 and Il1b[13,16,22-25] when compared to Gr-1+/CD11b+ cells from *Pten*$^{pc-/-}$ and *Pten*$^{pc-/-}$*;Trp53*$^{pc-/-}$ tumors (Fig. 2c and Supp. Fig. 4a). *Pten*$^{pc-/-}$*;Zbtb7a*$^{pc-/-}$ intra-tumoral Gr-1+/CD11b+ cells displayed a specific upregulation of these genes when compared to Gr-1+/CD11b+ cells from the peripheral blood (Supp. Fig. 4b) or to CD49f+ tumor cells (Supp. Fig. 4c).

We next assessed the expression levels of Il10[26] and Cd40[9,27], which are both associated with Treg cell function. Both genes were upregulated in Gr-1+/CD11b+ cells sorted from *Pten*$^{pc-/-}$*; Trp53*$^{pc-/-}$ tumors, when compared to those sorted from *Pten*$^{pc-/-}$*; Zbtb7a*$^{pc-/-}$ and *Pten*$^{pc-/-}$ tumors (Fig. 2d), suggesting genotype-specific modes of tumor promotion mediated by myeloid cells.

To further characterize the phenotype of these Gr-1+/CD11b+ cells we studied the expression of the Ly6G and Ly6C epitopes[21] (Fig. 2e and Supp. Fig. 4d). Flow cytometry analysis of primary tumors at 3 months of age revealed that CD11b+ cells in *Pten*$^{pc-/-}$*;Zbtb7a*$^{pc-/-}$ and *Pten*$^{pc-/-}$*;Trp53*$^{pc-/-}$ tumors were significantly different (Fig. 2e,f). While *Pten*$^{pc-/-}$*;Zbtb7a*$^{pc-/-}$

tumors contained primarily CD11b+/Ly6G+/Ly6C^{int} cells with immune phenotypic features of PMN-MDCSs/neutrophils[21,28], *Pten*$^{pc-/-}$*;Trp53*$^{pc-/-}$ tumors mainly recruit CD11b+/Ly6G-/Ly6C^{hi} cells with immune phenotypic features of Mo-MDSCs/monocytes[21]. At 6 months of age, the myeloid infiltrate of primary tumors in *Pten*$^{pc-/-}$*;Zbtb7a*$^{pc-/-}$ mice was still dominated by polymorphonuclear cells (Fig. 2g). By comparison, *Pten*$^{pc-/-}$*;Trp53*$^{pc-/-}$ CD11b+ cells showed an increase in CD11b+/Ly6G+/Ly6C^{int} cells accompanied by a slight decrease in the monocytic population, potentially secondary to differentiation of these cells into macrophages[29-31], which were markedly increased at this time point (Fig. 1f and 2f). In order to gain additional insights into the role of the monocytic and PMN populations detected in the *Pten*$^{pc-/-}$*;Trp53*$^{pc-/-}$ tumors at 3 months of age, we repeated the aforementioned gene expression analysis in CD11b+/Ly6G-/Ly6C^{hi} and CD11b+/Ly6G+/Ly6C^{int} sorted cells (Fig. 2h). The Ly6G+/Ly6C^{int} cells showed high expression of S100a8/a9 and Il1b, similar to the Gr-1+/CD11b+ cells collected from *Pten*$^{pc-/-}$*;Zbtb7a*$^{pc-/-}$ tumors, while the Ly6G-/Ly6C^{hi} population emerged as the primary contributor to the elevated levels of the immune suppressive genes Arg1, Il10 and Cd40.

Genotype specific chemokine expression pattern are directly influenced by gene loss in *Pten*$^{pc-/-}$*;Zbtb7a*$^{pc-/-}$ compared to *Pten*$^{pc-/-}$*;Trp53*$^{pc-/-}$ tumors.

To examine the mechanism of recruitment of Gr1+/CD11b+ cells, we initially analyzed our available microarray data set for expression of cytokines in *Pten*$^{pc-/-}$*;Zbtb7a*$^{pc-/-}$ compared to *Pten*$^{pc-/-}$ tumors[16]. Various cytokines were differentially regulated between the two models and loss of *Zbtb7a* in a *Pten* deficient setting leads to the upregulation of a very specific inflammatory program (Supp. Fig. 5a). In particular, Cxcl5, a member of the CXC-type chemokines and known attractant of granulocytic cells via Cxcr2[32-34], was one of the highest differentially regulated genes between *Pten*$^{pc-/-}$ and *Pten*$^{pc-/-}$*;Zbtb7a*$^{pc-/-}$ tumors (Supp. Fig. 5b). Expression analysis of selected chemokines from the CXC (Fig. 3a left) and the CC families (Fig. 3a right) in *Pten*$^{pc-/-}$, *Pten*$^{pc-/-}$*;Zbtb7a*$^{pc-/-}$ and *Pten*$^{pc-/-}$*;Trp53*$^{pc-/-}$ derived prostate tumors

validated that Cxcl5 was indeed specifically upregulated in *Pten*$^{pc-/-}$*;Zbtb7a*$^{pc-/-}$ tumors (Supp. Fig. 5c). Likewise, protein level of Cxcl5 was only increased in *Pten*$^{pc-/-}$*;Zbtb7a*$^{pc-/-}$ tumors (Fig. 3b).

As established by our own group and also by others, Zbtb7a is known to act as a transcriptional repressor[16,35,36]. Therefore, we hypothesized that Zbtb7a may transcriptionally suppress Cxcl5. Chromatin immunoprecipitation (ChIP) analysis of CXCL5 in RWPE-1 human immortalized prostate epithelial cells (Fig. 3c) confirmed that ZBTB7a is present on the CXCL5 locus and, consistent with this, overexpression of ZBTB7a led to downregulation of CXCL5 expression (Fig. 3d). Zbtb7a functions as a tumor suppressor in prostate cancer through the inhibition of Sox9 transcriptional activity that is elevated in Pten deficiency[16]. Accordingly, similar to the regulation of other Sox9 target genes, Cxcl5 was not upregulated in Pten sufficient *Zbtb7a*$^{pc-/-}$ prostates that lack high expression of Sox9 (Supp. Fig. 5d). Furthermore, knockdown of SOX9 by siRNA in RWPE1 cells suppressed the expression of CXCL5 whereas knockdown of ZBTB7a induced it (Fig. 3e). Lastly, we confirmed by ChIP that SOX9 is bound to the promoter of CXCL5 (Fig. 3f). Thus, we conclude that Zbtb7a can repress Cxcl5 gene expression through Sox9 inhibition and its loss in a *Pten* deficient setting leads to the overexpression of the Cxcl5 chemokine through increased Sox9 activity.

Our chemokine analysis further revealed a different pattern of inflammatory mediators in *Pten*$^{pc-/-}$*;Trp53*$^{pc-/-}$ tumors compared to *Pten*$^{pc-/-}$*;Zbtb7a*$^{pc-/-}$ tumors (Fig. 3a). Specifically, we found that Cxcl17, which was reported as an attractant for monocytic cells[37], was upregulated in *Pten*$^{pc-/-}$*; Trp53*$^{pc-/-}$ tumors as compared to the other models. Thus, similar to the regulation of CXCL5 by ZBTB7a, we next investigated whether p53 could transcriptionally suppress CXCL17. Intriguingly, knockdown of p53 expression by siRNA treatment in RWPE1 cells induced expression of CXCL17 (Fig. 3g) and ChIP analysis confirmed the ability of p53 to bind the promoter of CXCL17 (Fig. 3h). In summary, these data suggest that p53 differentially regulates

192 expression of CXCL17 in prostate epithelial cells, and the loss of p53 leads to the specific
193 upregulation of CXCL17 in *Pten$^{pc-/-}$; Trp53$^{pc-/-}$*.
194
195 **Differential mechanisms of Gr-1+/CD11b+ cell recruitment in *Pten$^{pc-/-}$;Zbtb7a$^{pc-/-}$* compared**
196 **to *Pten$^{pc-/-}$;Trp53$^{pc-/-}$* tumors.**
197 Immature myeloid cells that reside in the bone marrow can be induced to acquire phenotypic
198 features of MDSC upon addition of GM-CSF and interleukin-6 (IL6) to the culture medium[38]. To
199 analyze the potential role of CXCL5 and CXCL17 in shaping the TME, we first cultured mouse
200 bone marrow (BM) cells and Gr1+ cells isolated from the BM with IL6 and GM-CSF alone or in
201 the presence of either CXCL5 or CXCL17. After 4 days of culture we did not observe any
202 significant difference in the expression of the Ly6C and Ly6G markers or in the expression
203 profile of the genes tested (Fig. 4a and Supp. Fig. 6a,b), suggesting that these two chemokines
204 are not major determinants of immature myeloid cell phenotype. Nevertheless, in accordance
205 with previous studies[34,37], we were able to validate the function of CXCL5 and CXCL17 as
206 chemoattractants for PMN and monocytic cells, respectively. We performed a transwell
207 migration assay by using recombinant proteins and either Gr1+ cells (which are mostly
208 Ly6G+/Ly6C^{int} PMN cells) or monocytes isolated from the bone marrow of healthy mice (Supp.
209 Fig. 6c). CXCL5 strongly induced the migration of Gr1+ cells but not of monocytic Ly6G-/Ly6C^{hi}
210 cells (Fig. 4b), whereas CXCL17 showed a concentration-dependent effect only on monocytes
211 (Fig. 4c)[37].
212 Since there is currently no reliable anti-CXCL17 antibody available for *in vivo* neutralization
213 of mouse CXCL17, we sought to assess the role of Cxcl17 in *Pten$^{pc-/-}$;Trp53$^{pc-/-}$* tumors by
214 establishing organoid cultures. We isolated prostate cells from *Pten$^{pc-/-}$;Trp53$^{pc-/-}$*, *Pten$^{pc-/-}$*
215 *;Zbtb7a$^{pc-/-}$* and wild type mice and propagated them in vitro. Western blot analysis confirmed
216 that the genetically targeted tumor suppressor genes were almost completely absent (Fig. 4d).
217 Furthermore, IHC showed *Pten$^{pc-/-}$;Trp53$^{pc-/-}$*, *Pten$^{pc-/-}$;Zbtb7a$^{pc-/-}$* organoids with a histological

pattern similar to the mouse model of origin as well as elevated levels of both pAKT and Ki67 (Fig. 4e). Importantly, Cxcl17 expression was higher in the *Pten$^{pc-/-}$;Trp53$^{pc-/-}$* organoids, when compared to *Pten$^{pc-/-}$;Zbtb7a$^{pc-/-}$* and wild type (Fig. 4f).

Next, we performed a transwell migration assay using organoid conditioned medium (CM) and monocytes isolated from the bone marrow of 3 months old mice (Fig. 4g and Supp. Fig. 6c). In line with what we observed in prostate cancer mouse models, the migration of monocytic cells was greater using CM from *Pten$^{pc-/-}$;Trp53$^{pc-/-}$* organoids when compared to CM from *Pten$^{pc-/-}$;Zbtb7a$^{pc-/-}$* and wild type organoids (Fig. 4h). Notably, Cxcl17 stable knockdown in *Pten$^{pc-/-}$;Trp53$^{pc-/-}$* organoids (Fig. 4i) reduced the migration of monocytes to a degree that was similar to what we observed for *Pten$^{pc-/-}$;Zbtb7a$^{pc-/-}$* organoid CM (Fig. 4j and h), but had no effect on the migration of Gr1+ cells isolated from the BM (Fig. 4k).Collectively, our results support the idea that CXCL5 favors the infiltration of PMN myeloid cells in *Pten$^{pc-/-}$;Zbtb7a$^{pc-/-}$* tumors, while CXCL17 can be a chemoattractant for Mo-MDSCs in the *Pten$^{pc-/-}$;Trp53$^{pc-/-}$* model.

Selective blockade of Gr-1+/CD11b+ cells in *Pten$^{pc-/-}$;Zbtb7a$^{pc-/-}$* and *Pten$^{pc-/-}$;Trp53$^{pc-/-}$* impact tumorigenesis.

The identification of Gr-1+/CD11b+ cells as MDSCs is based on the functional evaluation of pro-tumoral, immune-mediated mechanisms. Based on our gene expression analysis, and on the presence of Treg cells in *Pten$^{pc-/-}$;Trp53$^{pc-/-}$* tumors (Fig. 5a), we performed *ex vivo* co-culture of CD4+ T cells with Gr1+/CD11b+ cells sorted from either *Pten$^{pc-/-}$;Trp53$^{pc-/-}$* or *Pten$^{pc-/-}$;Zbtb7a$^{pc-/-}$* tumors. Notably, only Gr1+/CD11b+ cells sorted from *Pten$^{pc-/-}$;Trp53$^{pc-/-}$* mice were able to induce the expansion of Treg cells (Fig. 5b). Therefore, in accordance with the recently published recommendation for MDSC nomenclature[21], we conclude that at 3 months of age the *Pten$^{pc-/-}$; Trp53$^{pc-/-}$* TME is characterized by the presence of Mo-MDSCs whereas *Pten$^{pc-/-}$;Zbtb7a$^{pc-/-}$* tumors are infiltrated by PMN-MDSC-like cells (PMN-MDSC-LC).

In order to validate our results *in vivo*, we initially tested the pro-tumoral activity of Gr-1+/CD11b+ cells by neutralizing CXCL5 in 3-4 months old *Pten*$^{pc-/-}$*;Zbtb7a*$^{pc-/-}$ mice, using an anti-mouse CXCL5 antibody. After 4 weeks of treatment we observed a reduction in tumor growth associated with a decrease of the intra-tumoral Gr-1+/CD11b+ cells (Fig. 5c and Supp. Table 1). The depletion of the myeloid infiltrate did not affect the number of Treg cells and did not result in an increase in CD8+ T cells (Fig. 5d), supporting our hypothesis that PMN cells that infiltrate *Pten*$^{pc-/-}$*;Zbtb7a*$^{pc-/-}$ are not immune suppressive and can therefore be classified as PMN-MDSC-LC. Additionally, similar results on tumor growth were obtained by the treatment of the *Pten*$^{pc-/-}$*;Zbtb7a*$^{pc-/-}$ mice with an anti-Ly6G depletion antibody[39] specific for PMN myeloid cells (Supp. Fig. 7a).

Next, to assess the role of Gr-1+/CD11b+ cells in the *Pten*$^{pc-/-}$*;Trp53*$^{pc-/-}$ model, we used an anti-Gr1 monoclonal antibody for the depletion of both Ly6G+ and Ly6C+ cells[40]. After 3 weeks of treatment, 3-4 months old mice showed a decrease in tumor growth and confirmed the depletion of intra-tumoral Gr-1+/CD11b+ cells (Fig. 5e and Supp. Table 1). Anti-Gr1 treated *Pten*$^{pc-/-}$*;Trp53*$^{pc-/-}$ mice displayed a decrease in Treg cells associated with an increase in CD8+ T cells (Fig. 5f). This analysis validates the *Pten*$^{pc-/-}$*;Trp53*$^{pc-/-}$ myeloid infiltrate as Mo-MDSCs.

Finally, we aimed to determine tumor growth rates upon CXCR2 antagonist SB225002 (CXCR2i) treatment, which is known to inhibit Gr-1+/CD11b+ cell attraction[41,42]. CXCR2 inhibition led to a decrease of Gr-1+/CD11b+ cells in all the models tested (Fig. 5g) and significantly suppressed the tumor growth of both *Pten*$^{pc-/-}$*;Zbtb7a*$^{pc-/-}$ and *Pten*$^{pc-/-}$*;Trp53*$^{pc-/-}$ but not the growth of the *Pten*$^{pc-/-}$*;Pml*$^{pc-/-}$ tumors (Fig. 5h and Supp. Table 1). Subsequent histological analysis in *Pten*$^{pc-/-}$*;Zbtb7a*$^{pc-/-}$ and *Pten*$^{pc-/-}$*;Trp53*$^{pc-/-}$ demonstrated that, while vehicle treated tumors displayed large tumor areas containing PIN lesions and complex glandular structures, the CXCR2 inhibitor treated mice displayed prostate glands with diminished tumor involvement and large tumor cysts (Supp. Fig. 7b). Moreover, *Pten*$^{pc-/-}$*; Trp53*$^{pc-/-}$ prostate tumors showed fewer Treg cells after treatment with SB225002 (Supp. Fig. 7c). Altogether, these data

confirm that Gr-1+/CD11b+ cells in *Pten$^{pc-/-}$;Zbtb7a$^{pc-/-}$* and *Pten$^{pc-/-}$;Trp53$^{pc-/-}$*, but not in the *Pten$^{pc-/-}$;Pml$^{pc-/-}$* tumors, exert a critical role in tumor progression and maintenance.

Gr-1+/CD11b+ cells in *Pten$^{pc-/-}$;Zbtb7a$^{pc-/-}$* promote tumor progression by impacting the NFkB signaling pathway.

Similar to *Pten$^{pc-/-}$;Zbtb7a$^{pc-/-}$* tumors, intratumoral PMN cells have recently been observed in a different mouse model of prostate cancer, the *Pten$^{pc-/-}$;Smad4$^{pc-/-}$*[34]. However, in that specific case, as well as in other tumor types[13], the PMN infiltrate displayed immunosuppressive activity. Therefore, we further investigated the mechanism by which PMN-MDSC-LCs promote *Pten$^{pc-/-}$;Zbtb7a$^{pc-/-}$* tumor growth. S100A9 was previously implicated in tumor progression through the upregulation of several pro-tumorigenic signaling pathways, including NFkB signaling through the activation of the RAGE/TLR4 receptors[43]. Similarly, IL1b is known as a regulator of inflammatory responses and as a pro-tumorigenic cytokine. It also activates NFkB signaling through its type 1 receptor[44]. In line with these published results, gene set enrichment analysis of microarray data obtained from *Pten$^{pc-/-}$* and *Pten$^{pc-/-}$;Zbtb7a$^{pc-/-}$* tumors shows an enrichment for NFkB target genes, specifically in *Pten$^{pc-/-}$;Zbtb7a$^{pc-/-}$* tumors (Supp. Fig. 8a), which we validated by western blot analysis showing increased pIRAK4 and decreased IkBa expression in *Pten$^{pc-/-}$;Zbtb7a$^{pc-/-}$* tumors (Supp. Fig. 8b). Conversely, western blot analysis of *Pten$^{pc-/-}$;Zbtb7a$^{pc-/-}$* tumors treated with the CXCR2i showed increased IkBa protein levels (Supp. Fig. 8c) as well as reduced expression of CXCL5, a known NFkB target gene (Supp. Fig. 8d). This result indicates a negative regulation of NFkB signaling after inhibition of Gr-1+/CD11b+ cell recruitment, and thereby links tumor promotive NFkB activation with Gr-1+/CD11b+ cell activity specifically in *Pten$^{pc-/-}$;Zbtb7a$^{pc-/-}$* tumors.

Validation of the association between tumor genotypes and differential immune-infiltrates in human samples.

Gene expression signatures have been shown to be an effective method to characterize the TME and can have a profound prognostic potential[45]. We took advantage of this approach to validate, in human samples, the association between CXCL5/17 and tumor-associated immune cells. To this end, we interrogated the 498 samples of The Cancer Genome Atlas (TGCA) provisional prostate adenocarcinoma dataset using a gene signature for PMN cells (PMN-Signature) and a gene signature for monocytic MDSCs and M2-like macrophages (Mo-Signature) (Methods and Supp. Table 2)[34,46]. The PMN signature clustered the TGCA samples into three groups: PMN-high, PMN-mid and PMN-low. In line with our findings in mouse model systems, CXCL5 expression was higher in the samples that showed high PMN-infiltrate signature (Fig. 6a). Similarly, the Mo-signature categorized the same dataset into the three groups Mo-high, Mo-mid and Mo-low (Fig. 6b). CXCL17 showed higher expression levels in the Mo-high group, consistent with our findings in mice

The concomitant deregulation of the tumor suppressor genes PTEN and TP53 is a common characteristic of advanced human prostate cancer[47] and we have recently shown that in patients with altered PTEN, low levels of Zbtb7a are associated with aggressive castration-resistant prostate cancer[18]. We therefore explored the possible link between these genetic make-ups and the expression of CXCL5 and CXCL17. To this end, we first examined a publicly available dataset of metastatic prostate cancer[47]. The cohort with PTEN altered (deleted or mutated) and ZBTB7A low expression status showed higher expression of CXCL5 (Fig. 6c), but not that of CXCL17. To investigate the human relevance of CXCL17 expression in prostate cancer, we focused our analysis on patient cohorts with different PTEN and p53 status. The cohort of PTEN alt; p53 alt (PTEN and TP53 deficiency based on homozygous deletion or mutations) patients showed the highest expression of CXCL17, whereas CXCL5 expression did not differ significantly among the different groups, consistent with our findings in mice (Fig. 6d).

Next, we focused our analysis on prostate cancer genetics vis a vis different immune landscapes. We used the aforementioned PMN-signature and a previously published T cell

signature[48] (Supp. Table 2) to categorize the metastatic prostate cancer samples of the Robinson dataset. The sequencing profiles were grouped into the high-, mid- and low-infiltrate clusters (Fig. 6e) and we analyzed how patients with genetics similar to the mouse models investigated in our study were distributed among the different groups. Remarkably, only 1 out of 9 patients with altered PTEN and Zbtb7a showed low PMN infiltrate and only 2 out of 18 PML deleted patients clustered into the PMN high type. Moreover, only 1 out of 18 samples PML deleted displayed high expression of the T cell-signature (Fig. 6f). Additionally, we analyzed PML expression levels in the different clusters. Significantly lower levels of PML expression were observed in the samples with less PMN and T-cell infiltrate (Fig.6g). Notably, the □-catenin and the MAPK signaling pathways have been directly linked to the "cold" TME phenotype[48-51], similar to what we observe in *Pten*$^{pc-/-}$;*Pml*$^{pc-/-}$ GEMMs. *Pten*$^{pc-/-}$;*Pml*$^{pc-/-}$ prostate cancers at 3 months of age showed upregulation of both □-catenin and phospho-ERK (Supp. Fig 9a). In summary, our findings from GEMMs and human cancer samples highlight the relevance of an integrated genotype-immuno-phenotype approach towards patient stratification.

Discussion

Diverse immune cell types can infiltrate and interact with solid and liquid tumors and can impact therapeutic approaches[11-13]. We hypothesized that distinct genomic alterations may shape the TME directly and differentially, through distinct mechanisms, based on distinct chemokine pools resulting from aberrant transcriptional and signaling programs.

We here demonstrate through a comparative analysis of models and mechanisms that the diverse genetics of prostate cancer can directly determine the differential infiltration and composition of immune cells in the TME (Fig. 6h and Supp. Fig. 9b). It has been shown that major tumor drivers (e.g. the RET/PTC rearrangement[52] or the loss of the SMAD tumor suppressor[34]) can activate proinflammatory and immune suppressive programs, and our comparative analysis now demonstrate that gene-specific intrinsic pathways are at the core of diverse pro-tumoral immune cell recruitment and infiltration**.**

Specifically, we show that Zbtb7a transcriptionally represses the granulocyte attractant CXCL5[32,34], which is upregulated in *Pten*$^{pc-/-}$*;Zbtb7a*$^{pc-/-}$ tumors, leading to an increased recruitment of PMN cells. In contrast, loss of p53 leads to upregulated expression of the known Gr-1+/CD11b cell attractant CXCL17[53]. In line with these findings, human prostate cancer specimens that express low levels of ZBTB7A and have altered PTEN show a significantly higher expression of CXCL5. Similarly, human prostate cancer specimens deficient for p53 and PTEN show a significantly higher expression of CXCL17.

We further show that tumor associated Gr-1+/CD11b+ cells exhibit a tumor-promoting phenotype in both *Pten*$^{pc-/-}$*;Zbtb7a*$^{pc-/-}$ as well as *Pten*$^{pc-/-}$*;p53*$^{pc-/-}$, albeit by distinct mechanisms. In *Pten*$^{pc-/-}$*;Zbtb7a*$^{pc-/-}$ tumors, infiltrating Gr-1+/CD11b+ cells exhibit a PMN-MDSC-LC phenotype[21] and can promote tumor progression directly by impacting the NFkB signaling pathway through the secretion of S100a9 and Il1b. In contrast, S100a9 expression and subsequent NFkB signaling activation is not upregulated in *Pten*$^{pc-/-}$*;p53*$^{pc-/-}$ tumors, which

primarily recruit Mo-MDSCs at an early stage. Accordingly, the tumor promoting impact of Gr-1+/CD11b+ cells in the *Pten*$^{pc-/-}$*;p53*$^{pc-/-}$ model is associated with Treg-mediated anti-tumor immune suppression (Fig. 6h and Supp. Fig. 9b). Notably, at a later stage, *Pten*$^{pc-/-}$*;p53*$^{pc-/-}$ tumors are primarily infiltrated by PMN-cells and macrophages which may derive from Mo-MDSCs[13].

In addition to the "tumor-promoting" immune landscape of the *Pten*$^{pc-/-}$*;Zbtb7a*$^{pc-/-}$ model and the "immuno-suppresive" phenotype of the *Pten*$^{pc-/-}$*;p53*$^{pc-/-}$ tumors, we describe here a third scenario: "the immune-desert" phenotype of *Pten*$^{pc-/-}$*;Pml*$^{pc-/-}$ prostate cancer, which mimics the "cold" phenotype observed in patients known to be resistant to anti-PD-L1/PD-1 therapy[14]. This model showed very limited intra-tumoral immune infiltration when compared to the other models, and did not respond to CXCR2i treatment. In keeping with these findings, and as a potential explanation for this phenotype, we recently associated the loss of *Pml* with decreased cytokine production[54], and we show upregulation of β-catenin and activation of the MAPK pathway, both implicated in suppressing anti-tumor immunity[48-51].

It is important to note that the genetic background of the mice can influence both tumorigenesis and immune response. A SNP analysis of the experimental models (see Supplementary Table 3), utilization of large experimental groups, mechanistic interrogation of the differential recruitment modalities, as well as validation in human cell lines and patient samples are therefore all required elements to assess differences and which we feel lend robustness to our analysis.

Our data regarding the qualitative difference of Gr-1+/CD11b+ cells attracted to prostate cancer may be especially relevant for tailoring immune therapies and for stratification of a responsive patient population. For example, while the combination of immune checkpoint inhibitors with MDSC-depleting strategies may be effective in patients with altered PTEN/TP53 and PTEN/SMAD4, it may not work as well in patients with altered PTEN/ZBTB7a or PTEN/PML. Likewise, the S100A9 inhibitor Tasquinimod that recently failed in a phase III

clinical trial in prostate cancer[55,56], may interfere with only a certain subpopulation of tumors recruiting S100A9 secreting Gr-1+/CD11b+ cells. In addition, CXCR2 antagonists are currently under investigation in clinical trials, and may be ineffective in tumors that do not recruit Gr-1+/CD11b+ cells.

These profound differences in immune landscapes among various cancer genotypes further highlight the need to thoroughly investigate and integrate these findings in the context of exploratory cancer treatments in preclinical settings. As an example, in a recent publication Patnaik et al. show the efficacy of the tyrosine kinase inhibitor Cabozantinib in a *Pten*$^{pc-/-}$;*p53*$^{pc-/-}$ mouse model, where a marked post-treatment recruitment of PMN cells was found critical for the anticancer response[57]. On the other hand, in a mouse model combining genetic loss of *Pten*, *p53* and *Smad4*, Cabozantinib treatment reduced the number of intra-tumoral PMN cells and this, in turn, greatly enhanced the anti-tumor efficacy of immune checkpoint blockade[58]. Thus, our comparative *in vivo* analysis provides experimental evidence to the notion that the genetics of cancer play a direct and critical role in shaping the cancer immune-phenotype and the outcome of combinatorial immunotherapy, strongly supporting the need for integrated genotypic-immune phenotypic analyses.

ACKNOWLEDGEMENTS

We thank the members of the Pandolfi Lab for critically reading and discussing the manuscript. We thank Nicole Pandell of the Preclinical Murine Pharmacogenetics Core at BIDMC, Kerri Burgess, Kelsey Berry and the members of the Center of Life Science animal facility for helping with all *in vivo* work. We thank the members of the Dana Farber Flow Cytometry Facility and BIDMC Flow Cytometry Core for the help with all cell sorting. We also thank the Small Animal Imaging Core at BIDMC for the MRI work. This work was funded by the NIH grant R01 CA102142 awarded to P.P.P and supported by a Jane Coffin Childs Postdoctoral Fellowship to M. B..

AUTHOR CONTRIBUTIONS

M. B., N. S., T. I., M. R., A. L. and P. P. P. designed the study; M. B., N. S., T. I. and M. R. developed methodology; M. B., N. S., T. I., M. R. and G. W. performed experiments; G. W., C. M., C. N., M. C., A. L., S. S. and J. G. C. provided administrative, technical or material support; N. S., T. I., C. N., J. K., A. L. and S. S. provided histology and immunohistochemistry; J. Z. performed bioinformatics analysis; M. B., N. S., T. I., M. R. and P. P. P. analyzed and interpreted data; M. B., N. S., T. I., M. R. and P. P. P. wrote the manuscript; P. P. P. supervised the study.

COMPETING FINANCIAL INTERESTS

The authors declare no competing financial interests.

References

1. Egeblad, M., Nakasone, E. S. & Werb, Z. Tumors as organs: complex tissues that interface with the entire organism. *Dev. Cell* **18,** 884–901 (2010).
2. Hanahan, D. & Coussens, L. M. Accessories to the Crime: Functionsof Cells Recruited to the Tumor Microenvironment. *Cancer Cell* **21,** 309–322 (2012).
3. Quail, D. F. & Joyce, J. A. Microenvironmental regulation of tumor progression and metastasis. *Nat. Med.* **19,** 1423–1437 (2013).
4. Nakasone, E. S. *et al.* Imaging tumor-stroma interactions during chemotherapy reveals contributions of the microenvironment to resistance. *Cancer Cell* **21,** 488–503 (2012).
5. Zou, W., Wolchok, J. D. & Chen, L. PD-L1 (B7-H1) and PD-1 pathway blockade for cancer therapy: Mechanisms, response biomarkers, and combinations. *Sci Transl Med* **8,** 328rv4–328rv4 (2016).
6. Small, E. J. *et al.* A pilot trial of CTLA-4 blockade with human anti-CTLA-4 in patients with hormone-refractory prostate cancer. *Clin. Cancer Res.* **13,** 1810–1815 (2007).
7. Slovin, S. F. *et al.* Ipilimumab alone or in combination with radiotherapy in metastatic castration-resistant prostate cancer: results from an open-label, multicenter phase I/II study. *Ann. Oncol.* **24,** 1813–1821 (2013).
8. Kwon, E. D. *et al.* Ipilimumab versus placebo after radiotherapy in patients with metastatic castration-resistant prostate cancer that had progressed after docetaxel chemotherapy (CA184-043): a multicentre, randomised, double-blind, phase 3 trial. *Lancet Oncol.* **15,** 700–712 (2014).
9. Gabrilovich, D. I., Ostrand-Rosenberg, S. & Bronte, V. Coordinated regulation of myeloid cells by tumours. *Nat Rev Immunol* **12,** 253–268 (2012).
10. Coffelt, S. B., Wellenstein, M. D. & de Visser, K. E. Neutrophils in cancer: neutral no more. *Nat Rev Cancer* **16,** 431–446 (2016).
11. Grivennikov, S. I., Greten, F. R. & Karin, M. Immunity, inflammation, and cancer. *Cell* **140,** 883–899 (2010).
12. Palucka, A. K. & Coussens, L. M. The Basis of Oncoimmunology. *Cell* **164,** 1233–1247 (2016).
13. Kumar, V., Patel, S., Tcyganov, E. & Gabrilovich, D. I. The Nature of Myeloid-Derived Suppressor Cells in the Tumor Microenvironment. *Trends in Immunology* **37,** 208–220 (2016).
14. Chen, D. S. & Mellman, I. Elements of cancer immunity and the cancer–immune set point. *Nature* **541,** 321–330 (2017).
15. Trotman, L. C. *et al.* Pten dose dictates cancer progression in the prostate. *Plos Biol* **1,** E59 (2003).
16. Wang, G. *et al.* Zbtb7a suppresses prostate cancer through repression of a Sox9-dependent pathway for cellular senescence bypass and tumor invasion. *Nat. Genet.* **45,** 739–746 (2013).
17. Chen, Z. *et al.* Crucial role of p53-dependent cellular senescence in suppression of Pten-deficient tumorigenesis. *Nature* **436,** 725–730 (2005).
18. Lunardi, A. *et al.* A co-clinical approach identifies mechanisms and potential therapies for androgen deprivation resistance in prostate cancer. *Nat. Genet.* **45,** 747–755 (2013).
19. Song, M. S., Salmena, L. & Pandolfi, P. P. The functions and regulation of the PTEN tumour suppressor. *Nat. Rev. Mol. Cell Biol.* **13,** 283–296 (2012).
20. Di Mitri, D. *et al.* Tumour-infiltrating Gr-1+ myeloid cells antagonize senescence in cancer. *Nature* **515,** 134–137 (2014).
21. Brandau, S. *et al.* Recommendations for myeloid-derived suppressor cell nomenclature and characterization standards. *Nature Communications* **7,** 1–10 (2016).

22. Garcia, A. J. *et al.* Pten null prostate epithelium promotes localized myeloid-derived suppressor cell expansion and immune suppression during tumor initiation and progression. *Mol. Cell. Biol.* **34,** 2017–2028 (2014).
23. Acharyya, S. *et al.* A CXCL1 paracrine network links cancer chemoresistance and metastasis. *Cell* **150,** 165–178 (2012).
24. Bruchard, M. *et al.* Chemotherapy-triggered cathepsin B release in myeloid-derived suppressor cells activates the Nlrp3 inflammasome and promotes tumor growth. *Nat. Med.* **19,** 57–64 (2013).
25. Bald, T. *et al.* Ultraviolet-radiation-induced inflammation promotes angiotropism and metastasis in melanoma. *Nature* **507,** 109–113 (2014).
26. Huang, B. *et al.* Gr-1+CD115+ immature myeloid suppressor cells mediate the development of tumor-induced T regulatory cells and T-cell anergy in tumor-bearing host. *Cancer Res.* **66,** 1123–1131 (2006).
27. Pan, P.-Y. *et al.* Immune stimulatory receptor CD40 is required for T-cell suppression and T regulatory cell activation mediated by myeloid-derived suppressor cells in cancer. *Cancer Res.* **70,** 99–108 (2010).
28. Kowanetz, M. *et al.* Granulocyte-colony stimulating factor promotes lung metastasis through mobilization of Ly6G+Ly6C+ granulocytes. *Proc. Natl. Acad. Sci. U.S.A.* **107,** 21248–21255 (2010).
29. Corzo, C. A. *et al.* HIF-1α regulates function and differentiation of myeloid-derived suppressor cells in the tumor microenvironment. *Journal of Experimental Medicine* **207,** 2439–2453 (2010).
30. Franklin, R. A. *et al.* The cellular and molecular origin of tumor-associated macrophages. *Science* **344,** 921–925 (2014).
31. Movahedi, K. *et al.* Different tumor microenvironments contain functionally distinct subsets of macrophages derived from Ly6C(high) monocytes. *Cancer Res.* **70,** 5728–5739 (2010).
32. Walz, A. *et al.* Structure and neutrophil-activating properties of a novel inflammatory peptide (ENA-78) with homology to interleukin 8. *Journal of Experimental Medicine* **174,** 1355–1362 (1991).
33. Koch, A. E. *et al.* Epithelial neutrophil activating peptide-78: a novel chemotactic cytokine for neutrophils in arthritis. *Journal of Clinical Investigation* **94,** 1012–1018 (1994).
34. Wang, G. *et al.* Targeting YAP-Dependent MDSC Infiltration Impairs Tumor Progression. *Cancer Discov* **6,** 80–95 (2016).
35. Kukita, A. *et al.* Osteoclast-derived zinc finger (OCZF) protein with POZ domain, a possible transcriptional repressor, is involved in osteoclastogenesis. *Blood* **94,** 1987–1997 (1999).
36. Maeda, T. *et al.* Role of the proto-oncogene Pokemon in cellular transformation and ARF repression. *Nature* **433,** 278–285 (2005).
37. Pisabarro, M. T. *et al.* Cutting Edge: Novel Human Dendritic Cell- and Monocyte-Attracting Chemokine-Like Protein Identified by Fold Recognition Methods. *The Journal of Immunology* **176,** 2069–2073 (2006).
38. Marigo, I. *et al.* Tumor-Induced Tolerance and Immune Suppression Depend on the C/EBPβ Transcription Factor. *Immunity* **32,** 790–802 (2010).
39. Daley, J. M., Thomay, A. A., Connolly, M. D., Reichner, J. S. & Albina, J. E. Use of Ly6G-specific monoclonal antibody to deplete neutrophils in mice. *Journal of Leukocyte Biology* **83,** 64–70 (2008).
40. Pekarek, L. A., Starr, B. A., Toledano, A. Y. & Schreiber, H. Inhibition of tumor growth by elimination of granulocytes. *Journal of Experimental Medicine* **181,** 435–440 (1995).
41. White, J. R. *et al.* Identification of a potent, selective non-peptide CXCR2 antagonist that inhibits interleukin-8-induced neutrophil migration. *J. Biol. Chem.* **273,** 10095–10098

(1998).
42. Stadtmann, A. & Zarbock, A. CXCR2: From Bench to Bedside. *Front Immunol* **3,** 263 (2012).
43. Markowitz, J. & Carson, W. E. Review of S100A9 biology and its role in cancer. *Biochim. Biophys. Acta* **1835,** 100–109 (2013).
44. Stylianou, E. & Saklatvala, J. Interleukin-1. *International Journal of Biochemistry and Cell Biology* **30,** 1075–1079 (1998).
45. Gentles, A. J. *et al.* The prognostic landscape of genes and infiltrating immune cells across human cancers. *Nat. Med.* 1–12 (2015). doi:10.1038/nm.3909
46. Ugel, S., De Sanctis, F., Mandruzzato, S. & Bronte, V. Tumor-induced myeloid deviation: when myeloid-derived suppressor cells meet tumor-associated macrophages. *Journal of Clinical Investigation* **125,** 3365–3376 (2015).
47. Robinson, D. *et al.* Integrative clinical genomics of advanced prostate cancer. *Cell* **161,** 1215–1228 (2015).
48. Spranger, S., Bao, R. & Gajewski, T. F. Melanoma-intrinsic β-catenin signalling prevents anti-tumour immunity. *Nature* **523,** 231–235 (2015).
49. Seliger, B. *et al.* Down-regulation of the MHC class I antigen-processing machinery after oncogenic transformation of murine fibroblasts. *Eur. J. Immunol.* **28,** 122–133 (1998).
50. Atkins, D. *et al.* MHC class I antigen processing pathway defects, ras mutations and disease stage in colorectal carcinoma. *Int. J. Cancer* **109,** 265–273 (2004).
51. Bradley, S. D. *et al.* BRAFV600E Co-opts a Conserved MHC Class I Internalization Pathway to Diminish Antigen Presentation and CD8+ T-cell Recognition of Melanoma. *Cancer Immunology Research* **3,** 602–609 (2015).
52. Borrello, M. G. *et al.* Induction of a proinflammatory program in normal human thyrocytes by the RET/PTC1 oncogene. *Proceedings of the National Academy of Sciences* **102,** 14825–14830 (2005).
53. Matsui, A. *et al.* CXCL17 expression by tumor cells recruits CD11b+Gr1 high F4/80- cells and promotes tumor progression. *PLoS ONE* **7,** e44080 (2012).
54. Lunardi, A. *et al.* A Role for PML in Innate Immunity. *Genes & Cancer* **2,** 10–19 (2011).
55. Williamson, S. C., Hartley, A. E. & Heer, R. A review of tasquinimod in the treatment of advanced prostate cancer. *Drug Des Devel Ther* **7,** 167–174 (2013).
56. Pili, R. *et al.* Phase II randomized, double-blind, placebo-controlled study of tasquinimod in men with minimally symptomatic metastatic castrate-resistant prostate cancer. *J. Clin. Oncol.* **29,** 4022–4028 (2011).
57. Patnaik, A. *et al.* Cabozantinib Eradicates Advanced Murine Prostate Cancer by Activating Anti-Tumor Innate Immunity. *Cancer Discov* CD–16–0778 (2017). doi:10.1158/2159-8290.CD-16-0778
58. Lu, X. *et al.* Effective combinatorial immunotherapy for castration-resistant prostate cancer. *Nature* **543,** 728–732 (2017).

Figure Legends

Figure 1. The genetic make-up of prostate cancer dictates the composition of immune infiltrates in the primary tumor. (**a**) Weight in grams of the prostates (anterior lobe) of controls (n=6), *Pten*$^{pc-/-}$ (n=4), *Pten*$^{pc-/-}$*;Zbtb7a*$^{pc-/-}$ (n=6), *Pten*$^{pc-/-}$*;Trp53*$^{pc-/-}$ (n=8), and *Pten*$^{pc-/-}$*;Pml*$^{pc-/-}$ (n=3), mice at 3 months of age. (**b**) Representative hematoxylin and eosin staining in the prostate tissues (anterior lobe) of controls, *Pten*$^{pc-/-}$, *Pten*$^{pc-/-}$*;Zbtb7a*$^{pc-/-}$, *Pten*$^{pc-/-}$*;Trp53*$^{pc-/-}$ and *Pten*$^{pc-/-}$*;Pml*$^{pc-/-}$ mice at 3 months of age (n=3 animals for each genotype with similar results). Black arrows show invasive sites. Scale bars, 0.1 mm. (**c**) Pie charts show percentage of T cells (CD45+/CD3+), B cells (CD45+/CD19+/B220+), Macrophages (CD45+/CD11b+/F4/80+) and CD45+/Gr-1+/CD11b+ cells in the prostate tissues of control mice and respective prostate tumor models at 3 months of age. 'Other cells' contains prostate epithelial cells and the other stromal cells. The number of mice used is indicated in Supp. Fig.1. (**d**) Summarized result of the CD45+/Gr-1+/CD11b+ immune cell population from (c). Number of mice used: control (n=4), *Pten*$^{pc-/-}$ (n=3), *Pten*$^{pc-/-}$*;Zbtb7a*$^{pc-/-}$ (n=6), *Pten*$^{pc-/-}$*;Trp53*$^{pc-/-}$ (n=7), and *Pten*$^{pc-/-}$*;Pml*$^{pc-/-}$ (n=4). (**e**) Weight in grams of the whole prostates of *Pten*$^{pc-/-}$*;Zbtb7a*$^{pc-/-}$ (n=6), *Pten*$^{pc-/-}$*;Trp53*$^{pc-/-}$ (n=10), and *Pten*$^{pc-/-}$*;Pml*$^{pc-/-}$ (n=3), mice at 6 months of age. (**f**) Pie charts as in (c) showing results collected from 6 months old mice. The number of mice used is indicated in Supp. Fig.2. All data in (a), (d) and (e) are represented as mean ± SEM. Values of $p<0.05$ were considered statistically significant. *P<0.05; **P<0.01; ***P<0.001 by two-tailed unpaired Student's t-test.

Figure 2. Characterization of Gr-1+/CD11b+ cells in *Pten*$^{pc-/-}$*;Zbtb7a*$^{pc-/-}$ and *Pten*$^{pc-/-}$*;Trp53*$^{pc-/-}$ prostate tumors. (**a**) May-Grunwald Giemsa staining of Gr-1+/CD11b+ cells sorted from *Pten*$^{pc-/-}$*;Zbtb7a*$^{pc-/-}$ and *Pten*$^{pc-/-}$*;Trp53*$^{pc-/-}$ prostate tumors (anterior prostate lobes, at 3 months of age). Experiment independently repeated two times with similar results. (**b**) Expression analysis of sorted intratumoral Gr-1+/CD11b+ cells from *Pten*$^{pc-/-}$ (n=3), *Pten*$^{pc-/-}$

622 *;Zbtb7a*$^{pc-/-}$ (n=3) or *Pten*$^{pc-/-}$*;Trp53*$^{pc-/-}$ (n=3) mice shows differential expressions of Arginase 1
623 and inducible nitric oxidase (iNOS). (**c**) Expression analysis of sorted intratumoral Gr-
624 1+/CD11b+ cells from *Pten*$^{pc-/-}$ (n=2), *Pten*$^{pc-/-}$*;Zbtb7a*$^{pc-/-}$ (n=3) or *Pten*$^{pc-/-}$*;Trp53*$^{pc-/-}$ (n=3) mice of
625 S100a9 and Il1□, and of (**d**) Il10 and Cd40. (**e**) Characterization of the Gr-1 epitopes, Ly-6G
626 and Ly-6C, in CD11b+ cells by flow cytometry and May-Grunwald Giemsa in *Pten*$^{pc-/-}$*;Zbtb7a*$^{pc-/-}$
627 and *Pten*$^{pc-/-}$*;Trp53*$^{pc-/-}$ tumors at 3 months of age. Experiment independently repeated two times
628 with similar results. (**f**) Quantification of the intratumoral Ly6G+/Ly6C+ and Ly6G-/Ly6C+ cell
629 populations at 3 months of age in *Pten*$^{pc-/-}$*;Zbtb7a*$^{pc-/-}$ (n=5) and *Pten*$^{pc-/-}$*;Trp53*$^{pc-/-}$ mice (n=5). (**g**)
630 Intratumoral Ly6G+/Ly6C+ and Ly6G-/Ly6C+ analysis in *Pten*$^{pc-/-}$*;Zbtb7a*$^{pc-/-}$ (n=6) and *Pten*$^{pc-/-}$
631 *;Trp53*$^{pc-/-}$ (n=6) mice at 6 months of age. (**h**) Expression analysis by qRT-PCR of sorted
632 intratumoral Ly6G+/Ly6C+ and Ly6G-/Ly6C+ cells from *Pten*$^{pc-/-}$*;Trp53*$^{pc-/-}$ mice (n=3). All data in
633 (b), (c), (d), (f), (g) and (h) are represented as mean ± SEM. Values of p<0.05 were considered
634 statistically significant. *P<0.05; **P<0.01; ***P<0.001 by two-tailed unpaired Student's t-test.
635
636 **Figure 3. Differential mechanisms of Gr-1+/CD11b+ cell recruitment in *Pten*$^{pc-/-}$*;Zbtb7a*$^{pc-/-}$**
637 **and *Pten*$^{pc-/-}$*;Trp53*$^{pc-/-}$ tumors.** (**a**) Expression analysis of chemokines in the prostate tumor
638 tissues (anterior lobes) of *Pten*$^{pc-/-}$(n=3), *Pten*$^{pc-/-}$*;Zbtb7a*$^{pc-/-}$(n=4) and *Pten*$^{pc-/-}$*;Trp53*$^{pc-/-}$(n=3)
639 mice at 3 months of age by qRT-PCR. Data are represented as mean ± SEM. Values of p<0.05
640 were considered statistically significant. *P<0.05; **P<0.01; ***P<0.001 by two-tailed unpaired
641 Student's t-test. (**b**) CXCL5 protein expression level in prostate tumors of *Pten*$^{pc-/-}$ (n=3) *Pten*$^{pc-/-}$
642 *;Zbtb7a*$^{pc-/-}$ (n=3) and *Pten*$^{pc-/-}$*;Trp53*$^{pc-/-}$ (n=3) mice at 3 months of age. Full scans of the blots are
643 in Supp. Figure 10a and b. (**c**) ChIP analysis in RWPE-1 human prostate epithelial cells shows
644 enrichment of CXCL5 locus in Zbtb7a immunoprecipitates, Mia and H19 serve as positive
645 controls. (**d**) Zbtb7a overexpression in RWPE-1 cells leads to a decrease of CXCL5 mRNA
646 levels. (**e**) Sox9 knockdown leads to a decrease of CXCL5 mRNA levels and Zbtb7a knockdown
647 leads to an increase of CXCL5 mRNA levels in RWPE-1 cells. (**f**) ChIP analysis in RWPE-1

cells shows enrichment of CXCL5 locus in Sox9 immunoprecipitates. (**g**) p53 knockdown in RWPE-1 cells leads to an increase of CXCL17 mRNA levels. p21 serves as a positive control. (**h**) ChIP analysis in RWPE-1 cells shows enrichment of CXCL17 locus in p53 immunoprecipitates, p21 serves as positive controls. All data in (c), (d), (e), (f), (g) and (h) are represented as mean of 3 cell culture experiments ± SEM. Values of $p<0.05$ were considered statistically significant. *P<0.05; **P<0.01; ***P<0.001 by two-tailed unpaired Student's t-test.

Figure 4. CXCL5 and CXCL17 are chemoattractant for PMN cells and monocytes respectively. (**a**) Ly6G+/Ly6C+ and Ly6G-/Ly6C+ flow analysis (n=3) of Gr1+ cells culture for 4 days in GM-CSF, IL-6 supplemented medium plus either recombinant CXCL5 or recombinant CXCL17. (**b**) Transwell migration assay of Gr1+ cells and (**c**) monocytes isolated form the bone marrow of healthy mice shows differential migration toward medium supplemented with increasing concentration of either recombinant CXCL5 or CXCL17 (n=3). (**d**) Western blot analysis confirms the specific deletion of the tumor suppressor genes Zbtb7a, PTEN and Trp53 in organoids isolated from our prostate cancer mouse models. Full scans of the blots are in Supp. Figure 10e-h. (**e**) H&E and IHC showing similar phopho-AKT and Ki67 staining in organoid generated from the prostates of 3 months old $Pten^{pc-/-};Zbtb7a^{pc-/-}$ and $Pten^{pc-/-};Trp53^{pc-/-}$ mice. (**f**) CXCL17 qRT-PCR expression analysis in organoids generated from the prostates of wild type, $Pten^{pc-/-};Zbtb7a^{pc-/-}$ and $Pten^{pc-/-};Trp53^{pc-/-}$ mice (n=3). (**g**) Schematic representation of the experimental strategy used to perform transwell migration assays using organoid conditioned medium. (**h**) Transwell migration assay of monocytes isolated from healthy mice shows increased migration toward conditioned medium from $Pten^{pc-/-};Trp53^{pc-/-}$ organoids (n=3). (**i**) CXCL17 qRT-PCR expression analysis in $Pten^{pc-/-};Trp53^{pc-/-}$ organoids shows the efficacy of the CXCL17 shRNA-mediated knockdown (n=3). (**j**) Reduced migration of monocytes (n=4), but not of Gr1+ cells (n=3) (**k**) in a transwell migration assay performed using conditioned medium from $Pten^{pc-/-};Trp53^{pc-/-}$ organoids expressing either scramble shRNA or a CXCL17 shRNA. All

674 data are represented as mean of cell culture replicates ± SEM. Values of p<0.05 were
675 considered statistically significant. *P<0.05; **P<0.01; ***P<0.001 by two-tailed unpaired
676 Student's t-test.
677
678 **Figure 5. Gr-1+/CD11b+ cells in *Pten$^{pc-/-}$;Zbtb7a$^{pc-/-}$* and *Pten$^{pc-/-}$;Trp53$^{pc-/-}$* prostate tumors**
679 **promote tumor growth.** (**a**) Flow cytometry analysis of CD4+/Foxp3+ cells in the prostate
680 tumors of *Pten$^{pc-/-}$; Zbtb7a$^{pc-/-}$* (n=3) and *Pten$^{pc-/-}$;Trp53$^{pc-/-}$* (n=3) mice at 3 months of age. (**b**)
681 Purified CD4+ T cells were co-cultured with Gr-1+/CD11b+ cells from *Pten$^{pc-/-}$;Zbtb7a$^{pc-/-}$* (n=3)
682 and *Pten$^{pc-/-}$;Trp53$^{pc-/-}$* (n=3) tumors for 3 days followed by flow cytometry to assess the presence
683 of CD4+/Foxp3+ Treg cells. (**c**) **Left panel**: measurement of tumor growth by MRI in *Pten$^{pc-/-}$*
684 *;Zbtb7a$^{pc-/-}$* mice treated with control IgG (n=7 mice) or anti-CXCL5 antibody (n=9 mice). **Middle**
685 **panel**: relative tumor growth of the mice showed in the left panel. **Right panel**: flow cytometry
686 analysis of intratumoral Gr-1+/CD11b+ in *Pten$^{pc-/-}$; Zbtb7a$^{pc-/-}$* prostate tumors after treatment
687 with either control IgG (n=9) or anti-CXCL5 antibody (n=8). (**d**) Flow cytometry analysis of
688 CD45+/CD8+ T cells (left) (n=5) and CD45+/CD4+/FoxP3+ Treg cells (n=5) in *Pten$^{pc-/-}$; Zbtb7a^{pc-}*
689 *$^{/-}$* prostate tumors after treatment with the anti-CXCL5. (**e) Left panel**: measurement of tumor
690 growth by MRI in *Pten$^{pc-/-}$;Trp53$^{pc-/-}$* mice treated with control IgG (n=4) or anti-Gr1 antibody
691 (n=4). **Middle panel**: relative tumor growth of the mice showed in the left panel. **Right panel**:
692 flow cytometry analysis of intratumoral Gr-1+/CD11b+ in *Pten$^{pc-/-}$; Trp53$^{pc-/-}$* prostate tumors after
693 treatment with either control IgG (n=4) or anti-Gr1 (n=5) antibody. (**f**) Flow cytometry analysis of
694 CD45+/CD8+ T cells (n=7) (left) and CD45+/CD4+/FoxP3+ Treg cells (n=5) in *Pten$^{pc-/-}$; Trp53$^{pc-/-}$*
695 prostate tumors after treatment with the anti-Gr1 antibody. (**g**) Flow cytometry analysis of *Pten^{pc-}*
696 *$^{/-}$; Zbtb7a$^{pc-/-}$* (n=6), *Pten$^{pc-/-}$;Trp53$^{pc-/-}$* (n=8), and *Pten$^{pc-/-}$;Pml$^{pc-/-}$* (n=4) prostate tumors after
697 treatment with the CXCR2 antagonist SB225002 (CXCR2i). (**h**) **Left panel**: Tumor growth
698 curves in vehicle (*Pten$^{pc-/-}$; Zbtb7a$^{pc-/-}$* (n=4), *Pten$^{pc-/-}$;Trp53$^{pc-/-}$* (n=4), and *Pten$^{pc-/-}$;Pml$^{pc-/-}$* (n=3))
699 or CXCR2i (*Pten$^{pc-/-}$; Zbtb7a$^{pc-/-}$* (n=6), *Pten$^{pc-/-}$;Trp53$^{pc-/-}$* (n=7), and *Pten$^{pc-/-}$;Pml$^{pc-/-}$* (n=3))

700 treated mice. **Middle panel**: relative tumor growth of the mice showed in the left panel. **Right**
701 **panel**: representative MRIs of prostate cancers in vehicle or CXCR2i treated mice of *Pten*$^{pc-/-}$
702 *;Zbtb7a*$^{pc-/-}$ at the indicated time point. Tumor volumes (area outlined by dotted red circle) were
703 quantified by using the PACS Imaging software. An asterisk represents the location of the
704 bladder. All data are represented as mean ± SEM. Values of $p<0.05$ were considered
705 statistically significant. *P<0.05; **P<0.01; ***P<0.001 by two-tailed unpaired Student's t-test.
706
707 **Figure 6. Clinical relevance of the genotype-chemokines-immuno phenotype axis of**
708 **prostate tumor models.** (**a**) Left panel: Heat map of the TGCA provisional prostate
709 adenocarcinoma dataset clustered into PMN-high (n=118), PMN-middle (n=206) and PMN-low
710 (n=174) groups using a gene signature for PMN-MDSCs. Right panel: CXCL5 is significantly
711 more expressed in the group of samples that showed higher expression of the PMN-signature.
712 (**b**) Left panel: Heat map of the TGCA provisional prostate adenocarcinoma dataset clustered
713 into Mo-high (n=171), Mo-middle (n=260) and Mo-low (n=67) groups using a gene signature for
714 monocytic MDSCs/M2 macrophages. Right panel: CXCL17 is significantly more expressed in
715 the group of samples that showed higher expression of the Mo-signature. (**c**) Expression level of
716 CXCL5 and CXCL17 in samples of the Robinson dataset (metastatic prostate cancer) grouped
717 by the status of PTEN (not altered/altered) and the expression level of Zbtb7a (low/high). The
718 number of samples in each group is indicated in the figure. (**d**) Expression level of CXCL17 and
719 CXCL5 in samples of the Robinson dataset grouped by the status of PTEN and p53 (not
720 altered/altered). The number of samples in each group is indicated in the figure. (**e**) Clustering
721 of the Robinson into the 3 groups PMN-high (n=34), PMN-mid (n=46) and PMN-low (n=37)
722 (upper panel), and into the 3 groups T cell-high (n=14), T cell-mid (n=33) and T cell-low (n=70)
723 (lower panel). (**f**) Distribution of patients with the indicated status of PTEN, p53, Zbtb7a and
724 PML in the different clusters generated by the PMN- and the T cell-signature in (e). (**g**) PML
725 expression level is significantly lower in the patients categorized in the PMN-low group and in

the T cell-low group when compared to the respective high-signature group. All data in (a), (b), (c), (d) and (g) are represented as box plots, interquartile range (IQR), and center line is the median (50% quantile). Whiskers define a range maximum to minimum excluding outliers (1.5 IQR outside considered as outliers). Values of $p<0.05$ were considered statistically significant. *P<0.05; **P<0.01; ***P<0.001 by two-tailed unpaired Student's t-test. (**h**) Immune phenotype model for tumor progression by Gr-1+/CD11b+ cells in *Pten*$^{pc-/-}$*;Zbtb7a*$^{pc-/-}$ and *Pten*$^{pc-/-}$*;Trp53*$^{pc-/-}$ mice.

ONLINE METHODS

Mice

Control, *Pten*$^{Lx/Lx}$;*Probasin-Cre* (referred to as *Pten*$^{pc-/-}$)[15], *Pten*$^{Lx/Lx}$;*Pml*$^{Lx/Lx}$ *Probasin-Cre* (referred to as *Pten*$^{pc-/-}$;*Pml*$^{pc-/-}$ manuscript in press), *Pten*$^{Lx/Lx}$;*Zbtb7a*$^{Lx/Lx}$ *Probasin-Cre* (referred to as *Pten*$^{pc-/-}$;*Zbtb7a*$^{pc-/-}$)[34] and *Pten*$^{Lx/Lx}$;*Trp53*$^{Lx/Lx}$ *Probasin-Cre* (referred to as *Pten*$^{pc-/-}$;*Trp53*$^{pc-/-}$)[17] mice were maintained in the animal facilities of Beth Israel Deaconess Medical Center (BIDMC)/Harvard Medical School in accordance with institutional rules and ethical guidelines for experimental animal care. All animal experiments were approved by the BIDMC IACUC protocol 066-2011 and 082-2014. The genetic background of the mice is described in the Supplementary Table 3.

In vivo drug and antibody treatments and MRI measurement

Mice were allocated at random to experimental groups. For flow analysis, all mice treated were 3 months of age. For treatment with the CXCR2 antagonist, SB225002 (Cayman Chemical #13336) was dissolved in DMSO (10 mg/ml) and diluted in vehicle (0.9% NaCl, 0.3% Tween 80) for *in vivo* administration. For MRI analysis, mice (3 to 5 months of age, Supp. Table 1) were treated daily for the indicated number of weeks by intraperitoneal injection (5 mg/kg). For depletion of Gr-1+/CD11b+ cells, Ly6G-depletion antibody (1A8, BioXcell) and control Rat IgG2a antibody (BioXcell) were diluted in phosphate-buffered saline (PBS) for *in vivo* administration. Mice (4 months of age) were treated every other day for 10 days by intraperitoneal injection (200-300 µg/mouse). InVivoMAb anti-mouse Ly6G/Ly6C (Gr-1) antibody, clone RB6-8C5 **(**BE0075, BioXcell), and control Rat IgG2b antibody (BE0090, BioXcell) were diluted in PBS and *Pten*$^{pc-/-}$;*Trp53*$^{pc-/-}$. Mice were treated every other day for 21 days by intraperitoneal injection (200 µg/mouse)**.** For neutralization of CXCL5, anti-Mouse CXCL5 antibody (Leinco Technologies) and control Rat IgG2a antibody (BioXcell) were diluted in PBS and injected every other day for 4 weeks by intraperitoneal injection (20 µg/mouse).

Tumor volume quantification was performed blinded to genotype and group allocation, by using VivoQuant and the PACS imaging software. All mouse prostate MRI imaging analysis were performed at Small Animal Imaging Core at BIDMC and acquired on an ASPECT Model M2 1T tabletop scanner.

Western Blot analysis and Immunohistochemistry

For western blotting, cell lysates were prepared by homogenizing tumor tissue with NP40 Buffer (Boston Bioproducts) supplemented with protease (Roche) and HALT phosphatase inhibitor cocktails (Thermo Scientific) and subsequently subjected to SDS-Gel separation (Invitrogen) and western blotting. The antibodies used for western blotting are listed in the "Life Sciences Reporting Summary". Western blots were quantified using Image J software.

For immunohistochemistry, tissues and organoids were fixed in 4% paraformaldehyde and embedded in paraffin in accordance with standard procedures. Embedding and hematoxylin and eosin staining of sections were performed by the Histology Core at BIDMC and analyzed by a pathologist. The antibodies used for immunohistochemistry are listed in the "Life Sciences Reporting Summary".

Cell lines and siRNA transfection

RWPE1 immortalized prostate epithelial cells were obtained from ATCC and tested for mycoplasma with the MycoAlert Mycoplasma Detection Kit (Lonza). RWPE1 cells were maintained in Keratinocyte Serum Free Medium supplemented with bovine pituitary extract (0.05 mg/ml) and human recombinant epidermal growth factor (5 ng/ml).

SiRNA targeting Zbtb7a, Sox9 and p53 (SIGMA; final 20 nmol/L) and non-target siRNA control (Thermo Fisher Scientific; final 20 nmol/L) were transfected into RWPE1 cells using Lipofectamine RNAiMAX (Invitrogen). After 48 hours, cells were subjected to mRNA expression analysis. Transient overexpression of Zbtb7a was done as previously described[25].

Chromatin Immunoprecipitation

Chromatin Immunoprecipitation (ChIP) was done using the Enzymatic Chromatin Immunoprecipitation Kit (Cell Signaling Technology # 9003) following manufacturer's recommendation. The antibodies used for the immunoprecipitation are listed in the "Life Sciences Reporting Summary". Analysis of immunoprecipitated DNA was done on the Step One Plus Real Time PCR System from Applied Biosystem using SYBR Green method. Fold Enrichment of ChIP experiments are shown. Primers for the detection of Mia and H19 loci are described previously[16]. Other genes were detected by:

CXCL5; forward Primer: ACAACGTCCCTCTCGGTAGA and reverse Primer: GGGCAGTGTGGAAAGAAGAG,

CXCL17; forward primer: CCAAGTTATCAGTCACCTTC and reverse primer: CATAACAGGTGAGGTGACGCTG,

p21; forward primer: GCTCCCTCATGGGCAAACTCACT and reverse primer: TGGCTGGTCTACCTGGCTCCTCT.

Organoid culture.

For the generation of mouse prostate cancer organoids, prostate cells were isolated and cultured as described by Drost and Karthaus et al.[59]. Briefly, the prostates of 3 months old mice were dissected and digested in a collagenase type II solution. Single cells were resuspeded in Matrigel and cultured as drops in complete prostate organoid medium (advanced DMEM/F12, GlutaMAX, penicillin-streptomycin, (DiHydro)testosterone, B27, N-acetylcystein, EGF, R-Spondin, Noggin, A83-01, Y27632).

Gr1+ cells and monocytes isolation, culture and migration assay.

Gr1+ cells and monocytes were isolated from the bone marrow (tibias and femurs) of C57BL/6

wild type, 3 months old mice using the MACS Myltenyi Biotec Cell Isolation system according to the manufacturer's instruction. For monocytes isolation the Monocyte Isolation Kit (BM) (Miltenyi 130-100-629) was used, whereas Gr1 positive cells were isolated using the antibody Anti-Gr-1-Biotin, clone RB6-8C5 (Miltenyi 130-101-894). Red blood cells were lysed with the ACK lysis buffer (ThermoFisher Scientific A1049201). Total bone marrow cells and Gr1+ cells were cultured for 4 days as described by Marigo et al.[38]. Briefly, 40 ng/ml GM-CSF (PeproTech #315-03) and 40 ng/ml IL-6 (PeproTech #216-16) were added to the control medium RPMI 1640 (ThermoFisher Scientific 11875-093) supplemented with penicillin-streptomycin, 10% FBS,10 mM HEPES, 20 μM 2-Mercaptoethanol. Either recombinant mouse CXCL5 (BioLegend #573302) or recombinant mouse CXCL17 (BioLegend #585402) was added at the beginning of the experiment (200nM). For the migration assay $2{,}5x10^5$ MACS sorted cells were resuspended in 100μL of either RPMI 1640 control medium or organoid complete medium and placed on the upper well of the transwell system (5μm, Corning #160241). The migration assay with recombinant proteins was performed by adding to the bottom well 600μL of RMPI1640 control medium supplemented with the indicated amount of either CXCL5 or CXCL17. The migration assay with organoid conditioned medium was performed by adding to the bottom well 600μL of medium collected over 5 days of culture of prostate organoids with the indicated genotype. The migration of cells was quantified by flow cytometry, 15 seconds acquisition time, using BD LSR II flow cytometer.

Cytospin

To perform Cytospins $2x10^5$ sorted granulocytes were resuspended in PBS containing 2% fetal bovine serum (FBS) (2% FBS/PBS) and spun onto slides with 250 rpm for 3 min in a slide centrifuge. Slides were subsequently fixed in methanol and stained with May Grunwald/GIEMSA.

Flow Cytometry

For Flow Cytometry spleen and lymph node single cell suspensions were prepared by mashing the tissue in 2% FBS/PBS. Tumor and control prostate tissue (from anterior lobes) single cell suspension was prepared by mincing the tumor and digestion with Collagenase Type I (Life Technologies # 17018029) in 10% DMEM (GIBCO) for 1hr at 37 °C. Cell suspensions were passed through 100 μM cell strainers to obtain single cell suspensions. Blood samples and single cell suspensions were re- suspended in 1-2 ml of ACK red cell lysis buffer (GIBCO) and lysed on ice for 1 minute. Cell suspensions were then washed in 2% FBS/PBS, centrifuged and re-suspended in 0.5-1 ml of 2% FBS/PBS. For flow cytometry, 100 μl of cell suspension was stained in a 96-well U-bottom plate. The antibodies used for flow cytometry are listed in the "Life Sciences Reporting Summary". All antibodies were used 1:100. To assess cell viability, cells were incubated with either DAPI or TO-PRO3 prior to FACS analysis. Foxp3 staining was done using FOXP3 Fix/Perm Buffer Set (BioLegend) and cells were stained by Foxp3-FITC antibody (eBioscience # 11-5773). All staining mixtures were analyzed on a BD LSR II flow cytometer (Becton Dickinson). Resulting profiles were further processed and analyzed using the FlowJo 8.7 software.

Cell sorting

For cell sorting of the intratumoral Ly6C+/Ly6G- and Ly6C+/Ly6G+ cell populations, and for Gr-1+/CD11b+ cell population, CD45-/CD49f+ cell population, CD4+ cell population, tumor tissue, blood and spleen was prepared as described above. After red blood cell lysis in 1-2 ml of ACK lysis buffer, cells were immunostained, washed and sorted on a BD^{TM} FACSAria II SORP cell sorter (Becton Dickinson). The antibodies used for cell sorting are listed in the "Life Sciences Reporting Summary".

***In vitro* Treg cells induction assay**

CD4+ T cells were sorted from spleen of tumor free control mice as described above. Purified CD4+ T cells were co-cultured with Gr1+/CD11b+ cells from *Pten*$^{pc-/-}$*;Zbtb7a*$^{pc-/-}$ and *Pten*$^{pc-/-}$*;Trp53*$^{pc-/-}$ tumors at 3 month of age at a ratio of 4:1 (T cells / Gr-1+/CD11b+ cells) in the presence of recombinant murine interleukin 2 (10 ng/ml, R&D Systems). After 4 days culture, cells were harvested and subjected to flow cytometry analysis as described above.

RT-PCR and microarray analysis

Microarray analysis and gene set enrichment analysis on mouse tumor tissue were conducted and analyzed as previously described[16]. For mRNA expression levels, tissue from indicated mice were homogenized in TRIZOL (Life Technologies #15596026) and RNA was extracted according to manufacturer's recommendation. RNA was further purified with the Pure Link RNA Mini Kit (Life Technologies #12183025) following the manufacturer's recommendation. For mRNA expression analysis of human cell lines or separated Gr-1 positive cells, RNA was isolated using Pure Link RNA Mini Kit following manufacturer's recommendations. RNA was reverse transcribed into cDNA by the High Capacity cDNA Reverse Transcription Kit (Life Technologies #4368814). Expression levels were measured via relative quantification on the Step One Plus Real Time PCR System from Applied Biosystem using SYBR Green method. Data are shown as fold change or expression values as indicated. Primer sequences are included in the Supplementary Table 4 and 5.

Gene Expression Profiling

The Cancer Genome Atlas Prostate Adenocarcinoma (TCGA-PRAD) data and Robinson metastatic prostate cancer data were downloaded from the cbioportal web site (http://www.cbioportal.org/)[60,61]. Normalized gene expression data were logarithm-transformed using base 2. Box plot and hierarchical clustering analyses were conducted with R programming. Samples with ZBTB7A expression below quantile 0.205 were counted low, above

quantile 0.795 counted as high. Samples with homozygous deletion of PTEN, TP53, or PML were counted as altered, “alt”. Standard t tests or Wilcoxon signed-rank tests were conducted to calculate the significance of number of samples falling into different categories in the boxplot. Z score test for two population proportions was conducted for fig 6f between the ratios, e.g. PMN-high ratio in PML-alt group versus that ratio in Pten-alt&Zbtb7a-low group.

We created signature gene set based on literature review. The genes used to generate the gene signatures used for our bioinformatics analysis are enlisted in Supplementary Table 2. The PMN signature and the Mo-MDSC signature have been generated by refining the MDSC gene signature used by Wang et al.[34]. The Wang et al. MDSC gene signature includes genes that can be expressed by either PMN-MDSCs or Mo-MDSCs, and genes expressed by Treg cells. Thus, on the basis of our own data, we removed from this list genes that we observed expressed by Mo-MDSCs in *Pten*$^{pc-/-}$*;Trp53*$^{pc-/-}$ tumors (i.e. Arg1, Il10, CD40), and genes expresses by Treg cells (i.e. FoxP3) to generate a Mo-MDSCs gene signature. The remaining genes in the Wang et al. MDSC gene signature were used to generate the PMN-MDSCs gene signature. Additional genes were added to the Mo-MDSCs gene signature by including Mo-MDSC and M2-like TAM human genes highlighted in the figure 1 of the review recently published by Bronte and colleagues[46]. The T cell-signature is the one used by Spranger et al.[48].

To identify the distribution pattern for each signature, we conducted hierarchical cluster using Euclidean distance. Patient samples were grouped together by the expression similarity of the signature gene set. After examining the topology of the clustering dendrogram, we obtained the number of major output partitions, which is three in this case. We then cut the tree to generate three clusters as reflected in the heatmap plot.

Statistical Analysis

No statistical method was used to predetermine sample size. For all statistical analyses GraphPad Prism 7 software was used and analysis were done by two-tailed unpaired Student's t-test. Values of $p<0.05$ were considered statistically significant. *P<0.05; **P<0.01; ***P<0.001.

Data availability

Any Supplementary Information and Source Data files are available in the online version of the paper and from the corresponding author upon request. The Microarray data have been already published[16] and accessioned with the Gene Expression Omnibus (GEO) under series GSE46473.

Methods-only references

59. Drost, J. *et al.* Organoid culture systems for prostate epithelial and cancer tissue. *Nat Protoc* **11,** 347–358 (2016).
60. Cerami, E. *et al.* The cBio cancer genomics portal: an open platform for exploring multidimensional cancer genomics data. *Cancer Discov* **2,** 401–404 (2012).
61. Gao, J. *et al.* Integrative analysis of complex cancer genomics and clinical profiles using the cBioPortal. *Science Signaling* **6,** pl1–pl1 (2013).

Bezzi et al., Figure 1

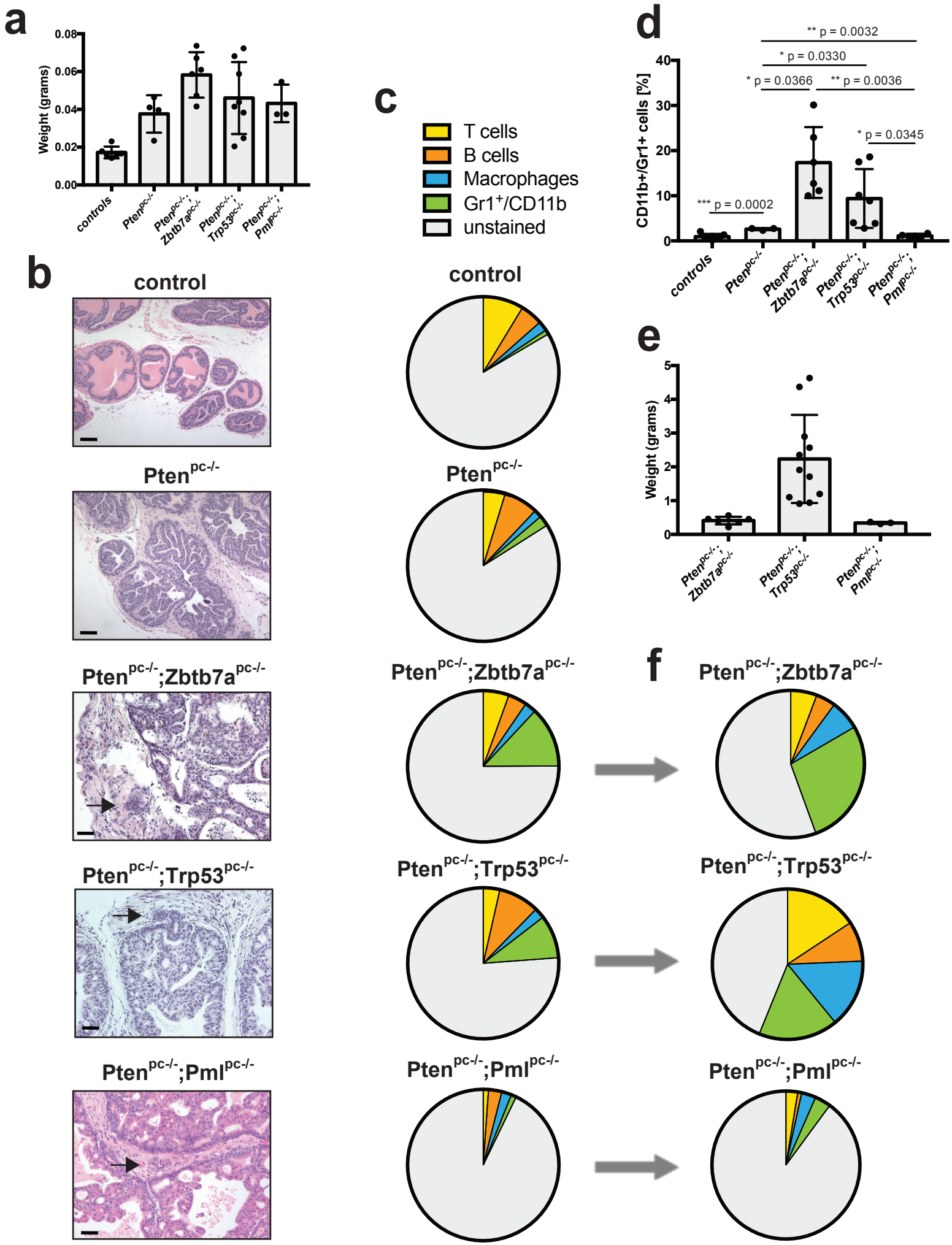

Bezzi et al., Figure 2

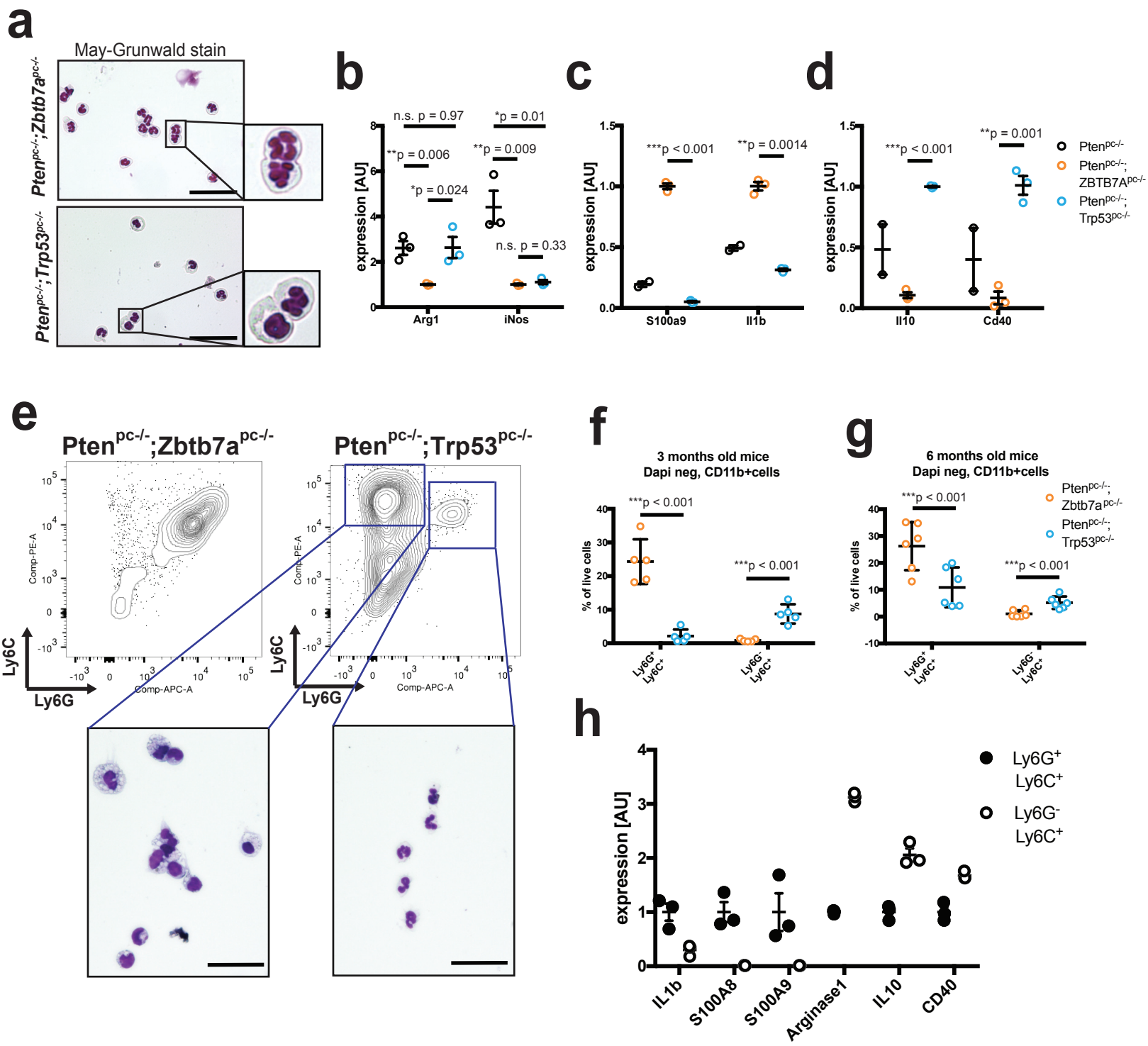

Bezzi et al., Figure 3

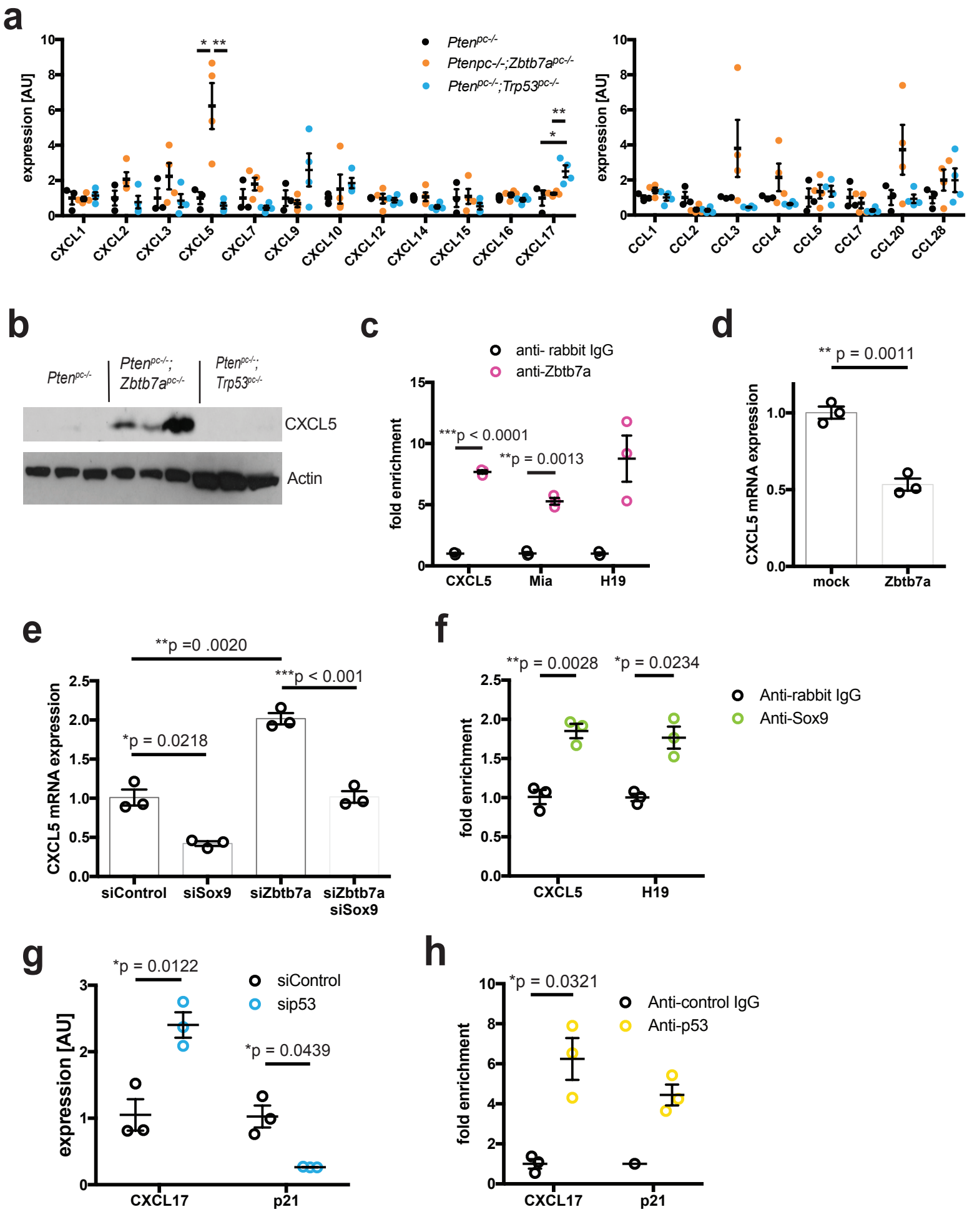

Bezzi et al., Figure 4

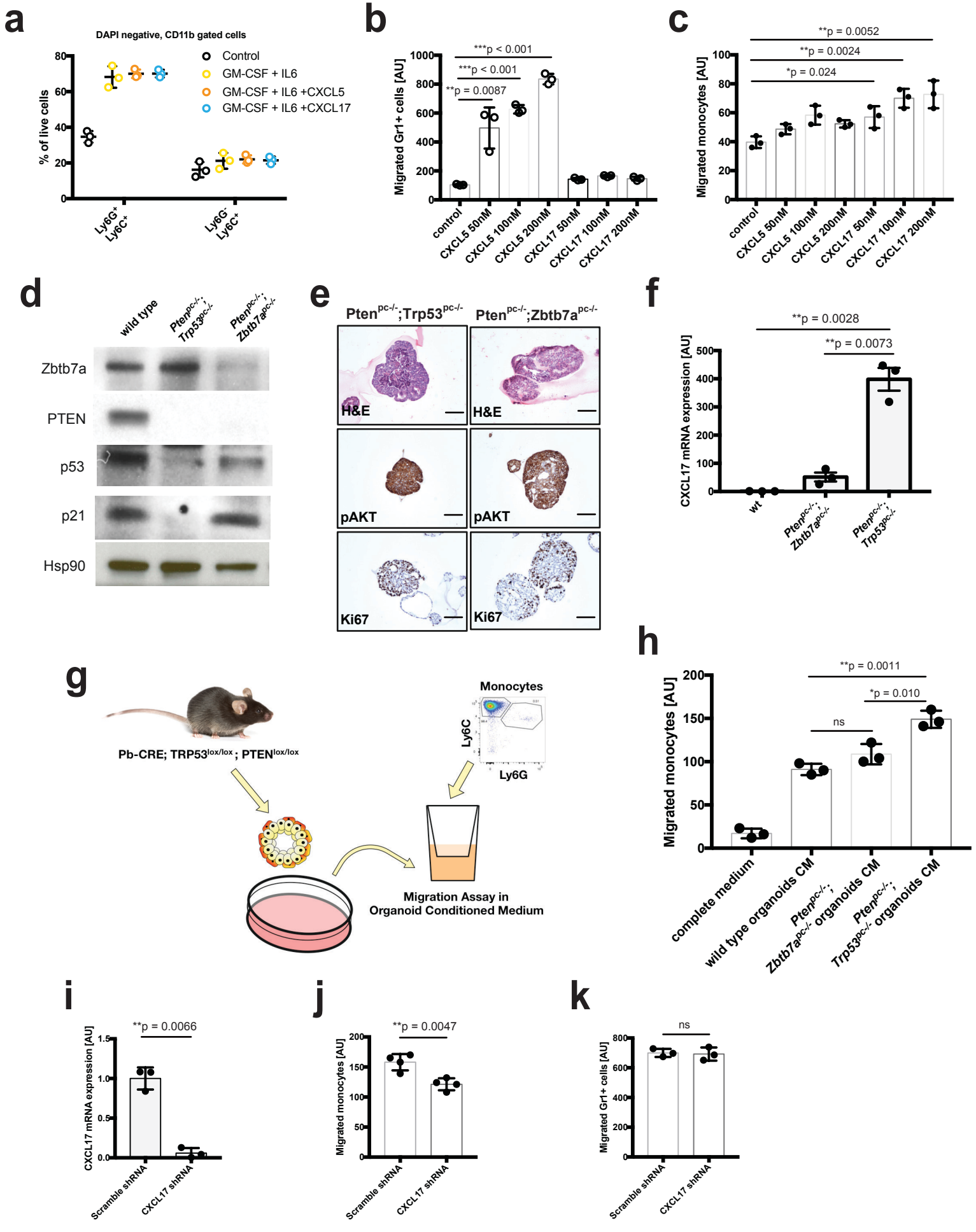

Bezzi et al., Figure 5

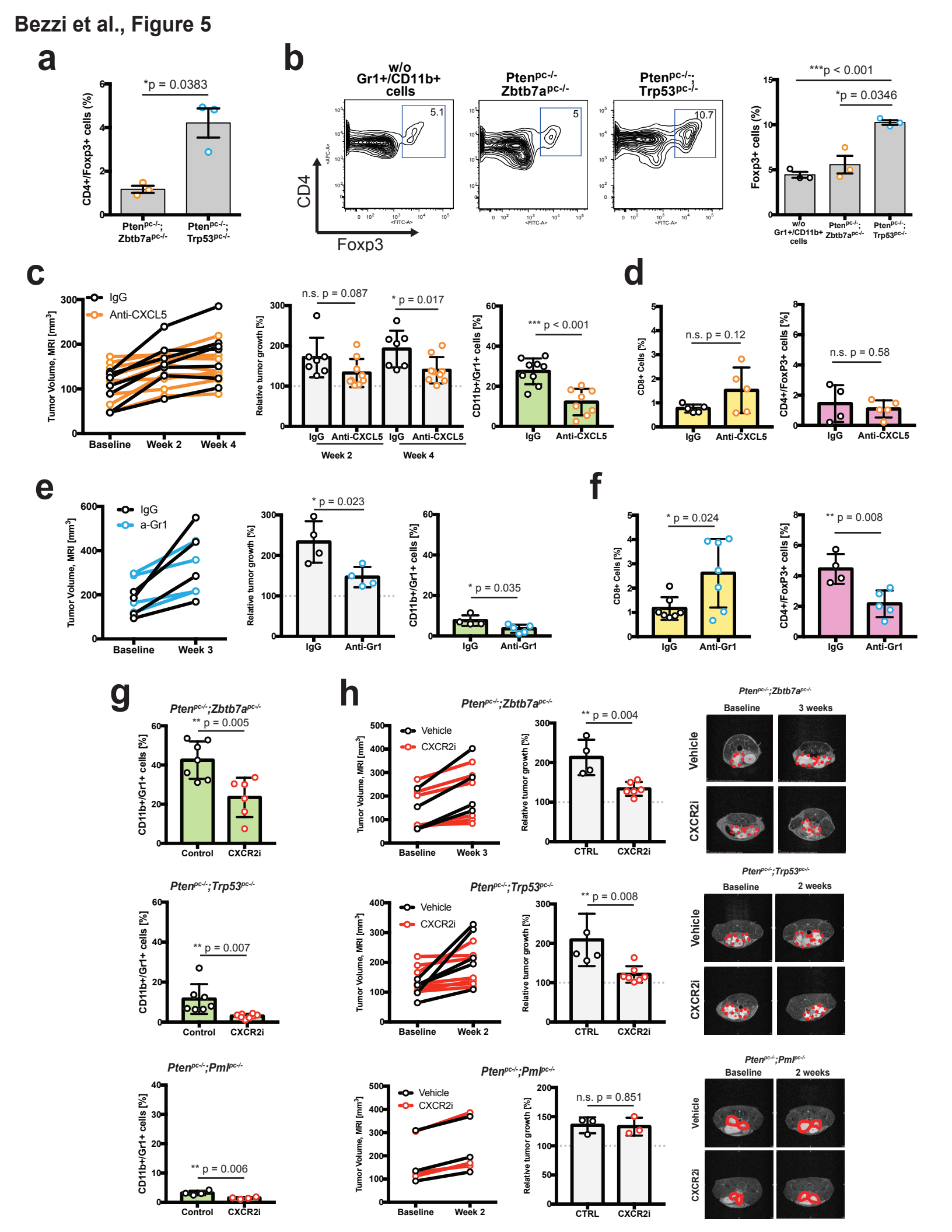

Bezzi et al., Figure 6